

# Green-Emitting Powders of Zero-Dimensional $\text{Cs}_4\text{PbBr}_6$ : Delineating the Intricacies of the Synthesis and the Origin of Photoluminescence

Aniruddha Ray,<sup>†,‡</sup> Daniela Maggioni,<sup>||</sup> Dmitry Baranov,<sup>†</sup> Zhiya Dang,<sup>†</sup> Mirko Prato,<sup>Δ</sup> Quinten A. Akkerman,<sup>†</sup> Luca Goldoni,<sup>⊥</sup> Enrico Caneva,<sup>§</sup> Liberato Manna,<sup>\*,†</sup> and Ahmed L. Abdelhady<sup>\*,†</sup>

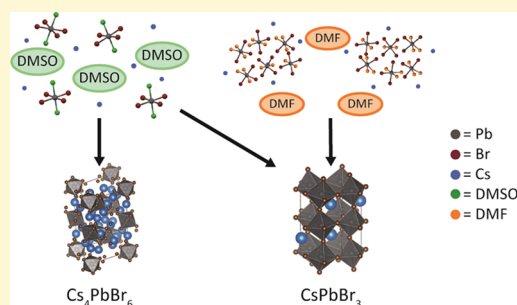
<sup>†</sup>Nanochemistry Department, <sup>Δ</sup>Materials Characterization Facility and <sup>⊥</sup>Analytical Chemistry Lab, Istituto Italiano di Tecnologia, Via Morego 30, 16163 Genova, Italy

<sup>‡</sup>Dipartimento di Chimica e Chimica Industriale, Università degli Studi di Genova, Via Dodecaneso 31, 16146 Genova, Italy

<sup>||</sup>Dipartimento di Chimica and <sup>§</sup>UNITECH COSPECT (Comprehensive Substance Characterization via Advanced Spectrometry), Università degli Studi di Milano, Via Golgi 19, 20133 Milano, Italy

## Supporting Information

**ABSTRACT:** A detailed investigation into the synthesis of green-emitting powders of  $\text{Cs}_4\text{PbBr}_6$  and  $\text{CsPbBr}_3$  materials by antisolvent precipitation from  $\text{CsBr}$ – $\text{PbBr}_2$  precursor solutions in dimethylformamide (DMF) and dimethyl sulfoxide (DMSO) is reported. Various solvated lead bromide and polybromide species ( $\text{PbBr}_2$ ,  $[\text{PbBr}_3]^-$ ,  $[\text{PbBr}_4]^{2-}$ , and possibly  $[\text{PbBr}_5]^{3-}$  or  $[\text{PbBr}_6]^{4-}$ ) are detected in the precursor solutions by optical absorbance and emission spectroscopies. The solvodynamic size of the species in solution is strongly solvent-dependent:  $\sim 1$  nm species were detected in DMSO, while significantly larger species were observed in DMF by dynamic light scattering. The solvodynamic size of the lead bromide species plays a critical role in determining the Cs–Pb–Br composition of the precipitated powders: smaller species favor the precipitation of  $\text{Cs}_4\text{PbBr}_6$ , while larger species template the formation of  $\text{CsPbBr}_3$  under identical experimental conditions. The powders have been characterized by  $^{133}\text{Cs}$  and  $^{207}\text{Pb}$  solid-state nuclear magnetic resonance, and  $^{133}\text{Cs}$  sensitivity toward the different Cs environments within  $\text{Cs}_4\text{PbBr}_6$  is demonstrated. Finally, the possible origins of green emission in  $\text{Cs}_4\text{PbBr}_6$  samples are discussed. It is proposed that a two-dimensional  $\text{Cs}_2\text{PbBr}_4$  inclusion may be responsible for green emission at  $\sim 520$  nm in addition to the widely acknowledged  $\text{CsPbBr}_3$  impurity, although we found no conclusive experimental evidence supporting such claims.



All-inorganic lead halide semiconductors have recently attracted renewed research interest due to the various stoichiometries that can be crystallized from the same precursors. Lead halide compounds demonstrate structural tunability based on the connectivity of the  $[\text{PbX}_6]^{4-}$  ( $X = \text{Cl}^-$ ,  $\text{Br}^-$ , or  $\text{I}^-$ ) octahedra that can form three-dimensional (3D) corner-sharing structures (perovskites), layered 2D networks, chains of 1D, and 0D isolated octahedral clusters.<sup>1–5</sup> In case of the organic–inorganic lead halide compounds, the size of the organic cation has been found to be one of the main factors determining the dimensionality of the octahedral framework. However, in the all-inorganic Cs–Pb–Br compounds, all three dimensionalities can be formed with the same Cs cation. Mixing  $\text{CsBr}$  and  $\text{PbBr}_2$  in specific ratios and in appropriate solvents leads to the formation of pure or mixed structures of  $\text{CsPbBr}_3$  (3D),  $\text{CsPb}_2\text{Br}_5$  (2D), and  $\text{Cs}_4\text{PbBr}_6$  (0D).<sup>6</sup>  $\text{PbBr}_2$ -rich conditions lead to the 2D tetragonal  $\text{CsPb}_2\text{Br}_5$  phase, characterized by a sandwich structure with  $\text{Cs}^+$  ions in between layers of  $[\text{Pb}_2\text{Br}_5]^-$ . On the other hand, under  $\text{CsBr}$ -rich conditions, a trigonal 0D  $\text{Cs}_4\text{PbBr}_6$  structure is formed, which consists of disconnected  $[\text{PbBr}_6]^{4-}$  octahedra separated by  $\text{Cs}^+$

ions. An equimolar amount or a slight excess of  $\text{PbBr}_2$  with respect to  $\text{CsBr}$  results in the formation of 3D  $\text{CsPbBr}_3$  with an orthorhombic structure of corner-sharing  $[\text{PbBr}_6]^{4-}$  octahedra, as in the organic–inorganic perovskites ( $\text{MAPbX}_3$  and  $\text{FAPbX}_3$ ; MA = methylammonium and FA = formamidinium) commonly used in optoelectronic applications.<sup>7</sup>

$\text{Cs}_4\text{PbBr}_6$ -based materials have recently gained increased interest due to the reports of strong and stable green photoluminescence (PL) in their powder, thin-film, single crystal, and nanocrystal forms.<sup>8–15</sup> However, it was reported that  $\text{Cs}_4\text{PbX}_6$  compounds are colorless<sup>16</sup> with band gaps in the UV region.<sup>12</sup> Specifically,  $\text{Cs}_4\text{PbBr}_6$  has a matching experimental and theoretical band gap around 3.95 eV.<sup>17–19</sup> Hence, the origin of the green PL has been proposed to be either due to intrinsic defects within the wide band gap of  $\text{Cs}_4\text{PbBr}_6$ <sup>13–15</sup> or due to the presence of 3D  $\text{CsPbBr}_3$  nanocrystals.<sup>19–24</sup> Ling et al.<sup>25</sup> suggested that the 3D  $\text{CsPbBr}_3$  phase is not the direct

Received: July 24, 2019

Revised: August 27, 2019

Published: August 28, 2019

cause of the intense PL; instead, they proposed trap states at the interface between the two phases (3D and 0D) to be responsible for that intense green emission.

Herein, we explore reaction parameters governing the formation of  $\text{Cs}_4\text{PbBr}_6$  and  $\text{CsPbBr}_3$  phases from  $\text{CsBr}$ – $\text{PbBr}_2$  solutions and the origin of the green PL in the  $\text{Cs}_4\text{PbBr}_6$  samples. The nature and solvodynamic size of the lead bromide species formed in solution varies with the coordination strength of the solvent and subsequently determines the composition of the formed Cs–Pb–Br powders: species with an  $\sim 1$  nm solvodynamic radius (presumably isolated octahedra) were detected in dimethyl sulfoxide (DMSO) solutions of  $\text{CsBr}$ – $\text{PbBr}_2$  leading to the formation of the  $\text{Cs}_4\text{PbBr}_6$  phase upon addition of an antisolvent, while larger species were detected in dimethylformamide (DMF) and resulted in the formation of the  $\text{CsPbBr}_3$  phase. In addition to the solvent, the solvent–antisolvent pair and the absolute concentrations of the precursors are key parameters defining the structure of the precipitated material. For example, antisolvents such as tetrahydrofuran (THF) and dichloromethane (DCM) precipitate mainly  $\text{Cs}_4\text{PbBr}_6$  and  $\text{CsPbBr}_3$  phases, respectively, from the  $\text{CsBr}$ – $\text{PbBr}_2$  solutions in DMSO when used in 1:6 (solvent:antisolvent by volume) ratios. Increasing the concentration of  $\text{CsBr}$ – $\text{PbBr}_2$  while keeping their molar ratio fixed (1:1) from 0.05 to 0.5 M in DMSO favors the formation of  $\text{CsPbBr}_3$  at higher concentrations. In addition to the powder X-ray diffraction (XRD) technique commonly used for a structural and compositional identification of the materials, we apply  $^{133}\text{Cs}$  and  $^{207}\text{Pb}$  solid-state nuclear magnetic resonance (ssNMR) to the analysis of various Cs–Pb–Br precipitates. We found that  $^{133}\text{Cs}$  ssNMR is more sensitive toward detecting relatively low impurity content of the different phases compared to its  $^{207}\text{Pb}$  counterpart. The  $^{133}\text{Cs}$  ssNMR results are in agreement with XRD data in terms of observed phases, but  $^{133}\text{Cs}$  ssNMR could also distinguish between the two different Cs crystallographic positions in the 0D crystal. Finally, based on the observed absorbance in the visible region and the recurring green PL of  $\text{Cs}_4\text{PbBr}_6$  samples, we hypothesize that 2D  $\text{Cs}_2\text{PbBr}_4$  inclusion (not observed experimentally) may be responsible for green PL in addition to the widely acknowledged 3D impurity.

## EXPERIMENTAL SECTION

**Materials.**  $\text{CsBr}$  (99.9%, Sigma-Aldrich),  $\text{PbBr}_2$  (98%, Sigma-Aldrich), DMSO (99.9%, Sigma-Aldrich), DMF (99.8%, Sigma-Aldrich), THF (99.9%, Sigma-Aldrich), and DCM (99.8%, amylene stabilizer, Sigma-Aldrich).

**Preparation of Cs–Pb–Br Powders.** Generally,  $\text{CsBr}$  and  $\text{PbBr}_2$  were dissolved in DMSO or DMF at the required ratio and at the required concentration by sonication for 1 h. Then, the solutions were filtered using a PTFE filter with 0.2 mm pore size, and the precipitation was carried out by quick injection of THF or DCM to the filtrate.

**Characterization.** The optical absorbance of the precursor solutions was recorded on a Varian Cary Eclipse UV–vis spectrophotometer. PLE and PL of precursor solutions were performed on a Varian Cary Eclipse fluorescence spectrophotometer. DLS was performed using a Zeta Sizer (Malvern Instruments) equipped with a 4.0 mW He–Ne laser operating at 633 nm and an avalanche photodiode detector in order to determine the average size of the precursors in the mother solution.

X-ray diffraction analysis was performed using a PANalytical Empyrean X-ray diffractometer equipped with a 1.8 kW Cu  $K\alpha$  ceramic X-ray tube and a PIXcel3D  $2 \times 2$  area detector, operating at 45 kV and 40 mA. Cs–Pb–Br powders were studied under ambient

conditions using a parallel beam in Bragg–Brentano geometry. XRD data was analyzed using HighScore 4.1 software from PANalytical. Step sizes of  $0.026^\circ$  and  $0.013^\circ$  and scan speeds of 0.102 and  $0.013^\circ/\text{s}$  were used for the standard and slow scans, respectively.

PL and PLQY measurements on dried powders were conducted on an Edinburgh Instruments FLS920 fluorescence spectrometer equipped with a calibrated integrating sphere exciting at 405 nm. Absorbance measurements for the powder samples were carried out in a Cary 5000 spectrometer using the diffuse reflectance accessory. Optical microscopy of the 4:1 DMSO powder was performed on a Nikon 80i microscope equipped with a grayscale digital camera, a high-pressure mercury lamp (Nikon), and optical filters. The sample was prepared by mixing a small amount of the finely ground powder with a drop ( $\sim 5 \mu\text{L}$ ) of octadecene-1. The mixture was prepared on top of a rectangular microscope slide and covered with a thin glass coverslip. Confocal PL microscopy on the same sample was performed using a Nikon A1 confocal laser microscope with 488 nm excitation (Oxxius LBX-488 diode laser). The laser power setting was kept at 0.5%, and the resolution of a 32-channel spectral detector was set at 2.5 nm during the experiments. The spectrally resolved imaging data and the z-series used for a volume view reconstruction (Figure S8) were acquired (as \*.ND2 files) using Nikon NIS-Elements High Content Software Analysis ver. 4.30.02 and viewed and processed in either Nikon NIS-Elements Viewer ver. 4.20.00 or ImageJ 1.51j8 as previously described.<sup>26</sup>

XPS measurements were carried out on a Kratos Axis UltraDLD spectrometer using a monochromatic Al  $K\alpha$  source (15 kV, 20 mA). The spectra were taken on a  $300 \times 700 \mu\text{m}^2$  area. Wide scans were collected with a constant pass energy of 160 eV and an energy step of 1 eV. High-resolution spectra were acquired at a constant pass energy of 10 eV and energy step of 0.1 eV. The binding energy scale was referenced to the C 1s peak at 284.8 eV. The spectra were analyzed using CasaXPS software (version 2.3.17). Samples were prepared by covering an indium substrate with the Cs–Pb–Br powder.

High-resolution transmission electron microscopy (HRTEM) analysis was carried out on a 200 kV TEM (JEOL JEM-2200FS) and a Bruker Quantax 400 system with an XFlash 5060 detector equipped on the same microscope was used for EDS analysis. The sample was prepared by dispersing the powders in THF before depositing on an ultrathin carbon film supported on holey carbon film-coated 400-mesh TEM copper grids.

Solid-state NMR (ssNMR) measurements were collected on a 500 MHz Bruker BioSpin NMR Spectrometer Avance 500, operating at a static field of 11.7 T and equipped with a 4 mm CPMAS probe by spinning the sample at the magic angle (MAS) with speed rates from 10 to 14 kHz. All samples were packed into zirconia ( $\text{ZrO}_2$ ) rotors and closed with Kel-F caps (80  $\mu\text{L}$  of internal volume). The working frequency of the  $^{133}\text{Cs}$  nucleus was 65.598 MHz, and spectra were acquired by using a single-pulse sequence (zg) with a spectral width of 104166 Hz, wide enough to ensure a homogeneous irradiation of the whole spectrum. The optimal spinning speed (MAS) was achieved at 10 KHz; however, comparative spectra were also acquired at different spinning rates (12 and 14 KHz) to assign all sidebands in the spectrum and to exclude any possible signal impurity overlapping the manifold SSB. The NMR parameters used for  $^{133}\text{Cs}$  experiments were  $90^\circ$  pulse length (p1) = 2.5  $\mu\text{s}$ , repetition time (d1) = 3–60 s, and number of scans (ns) = 200–800. The working frequency of the  $^{207}\text{Pb}$  nucleus was 104.63 MHz, and spectra were acquired by using a single-pulse sequence (solid echo with an echo time of 7  $\mu\text{s}$ ) with a spectral width of 1600 ppm (corresponding to 167.000 Hz), wide enough to allow a homogeneous irradiation of the whole spectrum but not enough to cover the wide anisotropic chemical shift range, typical of such a nucleus. Different experiments were needed (with the same spectral width but changing the offset) to cover the whole possible range of detectable signals. The spinning speed (MAS) was optimized at 10 kHz, a value that returned resolved spectra. The NMR parameters used for  $^{207}\text{Pb}$  experiments were the following:  $90^\circ$  pulse length (p1) = 2  $\mu\text{s}$ , repetition time (d1) = 0.5 s, and ns = 28.000–105.000.  $^{133}\text{Cs}$  and  $^{207}\text{Pb}$  shifts were referenced to solid  $\text{CsBr}$  ( $\delta_{\text{iso}} =$

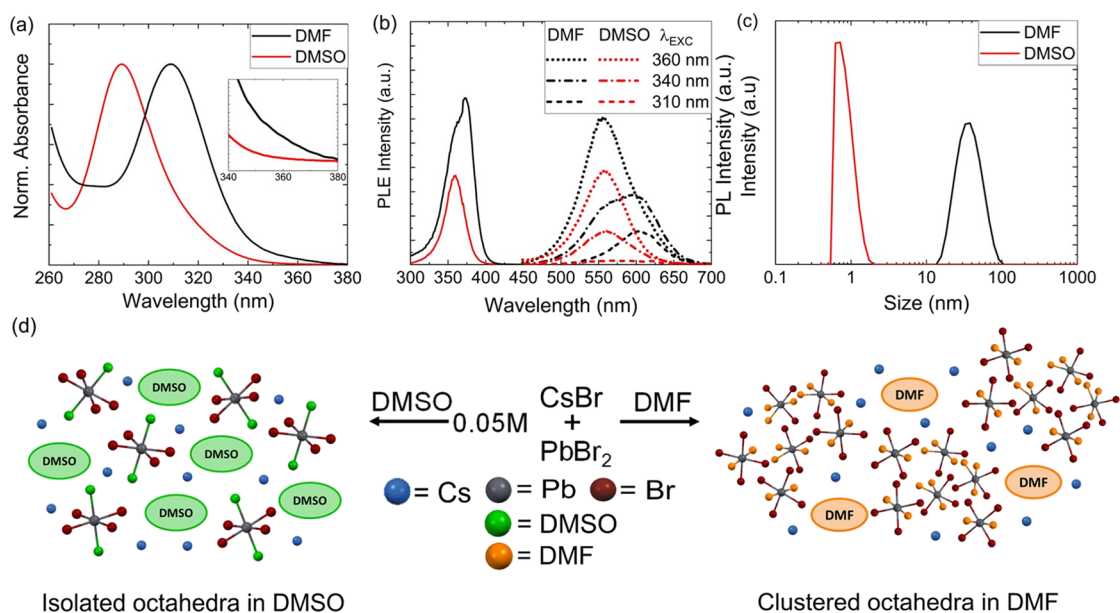


**Figure 1.** (a) Normalized absorbance and (b) PLE (solid lines) and PL (dotted and dashed lines) spectra of 0.05 M 1:1 CsBr:PbBr<sub>2</sub> precursor solutions in DMF and DMSO. PLE is reported at the highest intensity emission (560 nm), while PL is recorded at different excitation wavelengths. (c) Corresponding DLS measurements. (d) Scheme illustrating the photoactive species formed upon dissolving 0.05 M 1:1 CsBr:PbBr<sub>2</sub> in DMSO and DMF.

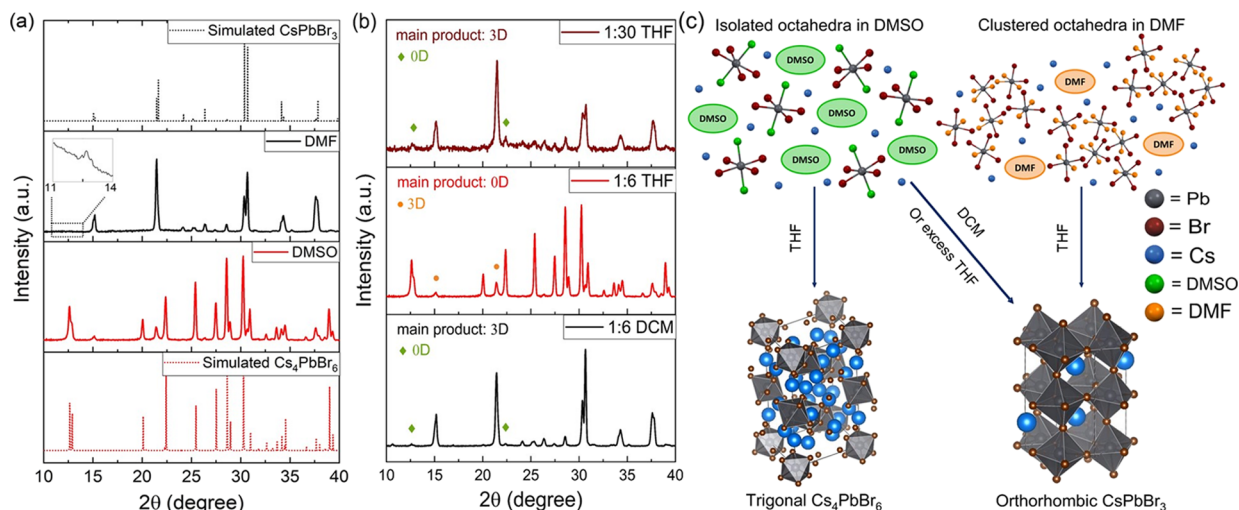


**Figure 2.** (a) XRD patterns of Cs-Pb-Br powders precipitated from 0.05 M 1:1 CsBr:PbBr<sub>2</sub> DMSO and DMF solutions along with simulated patterns for trigonal Cs<sub>4</sub>PbBr<sub>6</sub> (ICSD-162158) and orthorhombic CsPbBr<sub>3</sub> (ICSD-97851) phases. (b) XRD of Cs-Pb-Br powders precipitated from different DMSO:antisolvent volume ratios. (c) Scheme illustrating the effect of the solvodynamic size and solvent-antisolvent pair on the formed phases.

268.0 ppm vs CsCl:  $\delta_{\text{iso}} = 223.2$  ppm) and Pb(NO<sub>3</sub>)<sub>2</sub> ( $\delta = -3490$  ppm), respectively, which were used as external calibration standards.

## RESULTS AND DISCUSSION

**CsBr-PbBr<sub>2</sub> Solutions in DMSO and DMF.** PbBr<sub>2</sub>-containing solutions in DMF and DMSO are precursors for the Cs<sub>4</sub>PbBr<sub>6</sub> and CsPbBr<sub>3</sub> samples; thus, it is anticipated that the nature of the solvated species has an effect on the resulting material obtained from them. Steady-state optical spectroscopy is a simple method for investigation of the lead bromide speciation. Absorbance, photoluminescence (PL), and photoluminescence excitation (PLE) spectra of 0.05 M solutions of CsBr:PbBr<sub>2</sub> mixtures (1:1 molar ratio) in DMSO and DMF were collected and are reported in Figure 1. The DMSO

solution showed an absorbance peak at 285 nm that is attributed to PbBr<sub>2</sub>, while the DMF solution had a clear absorbance peak at 310 nm corresponding to [PbBr<sub>3</sub>]<sup>-</sup> (Figure 1a), consistent with previous studies.<sup>27,28</sup> Both solutions showed an absorbance tail in the longer wavelength region (340–360 nm, inset in Figure 1a), suggesting the possible formation of [PbBr<sub>4</sub>]<sup>2-</sup> species.<sup>27</sup> Both [PbBr<sub>3</sub>]<sup>-</sup> and [PbBr<sub>4</sub>]<sup>2-</sup> species are emissive (at ~600 and 560 nm, respectively),<sup>27,28</sup> and their presence can be confirmed through selective wavelength excitation (Figure 1b). The DMSO solution emitted at 560 nm regardless of the excitation wavelength, indicating the presence of mainly [PbBr<sub>4</sub>]<sup>2-</sup>. On the other hand, the DMF solution exhibited emissions at 560 and 600 nm, confirming the presence of detectable amounts of

both  $[\text{PbBr}_3]^-$  and  $[\text{PbBr}_4]^{2-}$  species. A relatively higher PL intensity of the DMF solution compared to DMSO under 360 nm excitation (Figure 1b) suggests a relatively higher concentration of  $[\text{PbBr}_4]^{2-}$  species in DMF with respect to DMSO (consistent with a higher absorbance at around 360 nm). The presence of an extra PLE peak at 374 nm in the DMF solution (Figure 1b) that is redshifted relative to that of  $[\text{PbBr}_4]^{2-}$  in the DMSO solution suggests that higher-order lead polybromide complexes, such as  $[\text{PbBr}_5]^{3-}$  or  $[\text{PbBr}_6]^{4-}$ , might be present in DMF (by analogy with their iodide counterparts).<sup>29</sup>

We performed DLS measurements on both solutions to further investigate the discussed differences in lead bromide speciation between the two solvents. It was found that the DMSO solution contained roughly 1 nm-sized lead bromide species, while the DMF solution was composed of significantly larger clusters (Figure 1c). The large-sized clusters in the DMF solution could be due to an aggregation or polymerization of the lead bromide species because of the different solvent–solute interaction between  $\text{PbBr}_2$  and DMF compared to DMSO (similar to  $\text{PbI}_2$ ).<sup>29–31</sup> Our findings indicate that a change of solvent significantly alters the speciation and the solvodynamic size of the lead bromide species, as schematically summarized in Figure 1d. The results hold in the absence of CsBr, as summarized in the Supporting Information (see Figure S1 and accompanying discussion). Previously, the changes in the solvodynamic size of the lead polyhalide species have been attributed to the relative ratio of salts (e.g., MAI: $\text{PbI}_2$ ; MA = methylammonium)<sup>32</sup> or to the effect of additives such as hydrohalic acids.<sup>33</sup> This is of high significance to the perovskite photovoltaic community as the solvodynamic size of the species present in the precursor solution influences the composition of the resulting material (see below) and subsequent optoelectronic properties of the devices.<sup>32,33</sup>

**$\text{Cs}_4\text{PbBr}_6$  and  $\text{CsPbBr}_3$  Formation.** Next, we investigated the differences in the composition of the powders precipitated from the abovementioned CsBr– $\text{PbBr}_2$  solutions in DMSO and DMF. Using the equimolar (0.05 M each precursor) solutions in DMSO and DMF, the precipitation of the powders was done by a quick injection of 6 mL of tetrahydrofuran (THF) to 1 mL of the solution. Powders were then dried overnight in a vacuum oven at 40 °C. X-ray diffraction (XRD) patterns of the dried powders are plotted in Figure 2a along with the simulated patterns of  $\text{Cs}_4\text{PbBr}_6$  and  $\text{CsPbBr}_3$ . It is observed that mainly the 0D trigonal phase was obtained from the DMSO solution with only low-intensity peaks corresponding to a 3D impurity, while 3D  $\text{CsPbBr}_3$  was the main precipitate from the DMF solution with an extremely low contamination from the 0D phase (inset in Figure 2a). The 0D impurity was only detected upon performing a slow XRD scan (see Experimental Section). We could eliminate the 0D impurity by using a CsBr: $\text{PbBr}_2$  ratio of 1:1.2 in DMF. This is relevant for perovskite-based light-emitting devices as we observed that even this extremely small amount of 0D impurity in the 3D sample could significantly enhance the PL peak (Figure S2). The differences in the compositions obtained from DMSO (mainly  $\text{Cs}_4\text{PbBr}_6$ ) and DMF (mainly  $\text{CsPbBr}_3$ ) under identical precipitation conditions can be rationalized on the basis of the DLS data of the precursor solutions (Figure 1c). The formation of clusters of the lead bromide species in the DMF solution possibly templates the growth of the 3D orthorhombic phase upon the addition of the antisolvent. On the other hand, the ~1 nm-sized particles in DMSO, which are

in agreement with a previous report,<sup>34</sup> suggest that most of the complexes in solution are isolated octahedra, making the crystallization of the 3D phase less favorable. Coordination strength of the solvent is likely a main factor responsible for these differences. DMSO is known to have a stronger coordination with  $\text{Pb}^{2+}$  compared to DMF;<sup>30</sup> hence, the Cs-rich phase  $\text{Cs}_4\text{PbBr}_6$  can be easily precipitated from DMSO solution while the composition of precipitates from DMF solution is closer to the stoichiometry of the feed solution (1:1 CsBr: $\text{PbBr}_2$ ). Nonetheless, 3D  $\text{CsPbBr}_3$  could be precipitated out from a DMSO solution by changing the antisolvent or the absolute concentration of the precursors, as discussed next.

We studied the effect of two different antisolvents on an equimolar (0.05 M) mixture of CsBr and  $\text{PbBr}_2$  dissolved in DMSO. THF and dichloromethane (DCM) were chosen as antisolvents. XRD patterns of the powders are presented in Figure 2b. Simply by changing the antisolvent from THF (1:6 THF) to DCM (1:6 DCM), despite the absence of any large-sized clusters, 3D perovskite is the main precipitate (see sketches in Figure 2c). Hence, it is not only the solvodynamic size of the different lead polybromide in the precursor solution that controls the phase of the obtained precipitate but also the solvent–antisolvent pair. In a 1:1 CsBr: $\text{PbBr}_2$  DMSO solution, addition of THF favors the precipitation of the Cs-rich phase ( $\text{Cs}_4\text{PbBr}_6$ ) possibly due to the higher solubility of  $\text{PbBr}_2$ , compared to CsBr, in this solvent–antisolvent pair. On the other hand, using DCM as an antisolvent resulted in the precipitation of the 3D phase as both precursors are relatively insoluble in the DMSO–DCM pair. Nevertheless, when an excess amount of THF is added (1:30 THF), the 3D phase is the primary formed phase (see Figure 2b). It could be possible that excess THF forces full precipitation of the  $\text{PbBr}_2$  present in the precursor solution; hence, the stoichiometric 3D phase is formed. The effect of the solvodynamic size of the different lead polybromide species and solvent–antisolvent pair on the resulting Cs–Pb–Br phase is demonstrated in Figure 2c. We also explored a mixed DMSO/DMF solution and found that both THF and DCM lead to the precipitation of mainly the 3D phase with minor 0D impurity (Figure S3). Another parameter that we varied was the absolute concentration of the solution (0.05 to 0.5 M) using DMSO–THF as the solvent–antisolvent pair, and interestingly, we discovered that the lower concentration favors the precipitation of a majority of 0D, while the higher concentration favors a majority of 3D perovskites (Figure S4). The 3D precipitated from the 0.5 M DMSO solution is likely due to the high concentration that results in significant interaction between adjacent octahedra after the addition of the antisolvent.<sup>35</sup> In fact, upon direct addition of the antisolvent, we observed a white precipitate, which is most probably in the 0D phase or ultrasmall 3D clusters<sup>36</sup> that in a few seconds turned into orange-colored 3D perovskites.

XRD analysis of the precipitate from the lower absolute concentration (0.05 M) detected around 15% 3D  $\text{CsPbBr}_3$  (see Note S1); hence, we used a 4:1 CsBr: $\text{PbBr}_2$  ratio in order to precipitate 3D-free 0D  $\text{Cs}_4\text{PbBr}_6$  (Figure 3, blue pattern). We observed that the (121) peak at  $21.5^\circ$  ( $2\theta$ ) corresponding to the 3D orthorhombic phase completely disappeared. However, at this precursor ratio, peaks, especially the (110) peak at  $29.5^\circ$  ( $2\theta$ ), corresponding to cubic CsBr are detected. Importantly, powders precipitated from 3.75:1 CsBr: $\text{PbBr}_2$  contained detectable 3D impurity (Figure 3, green pattern). These results suggest that the formation of CsBr- and

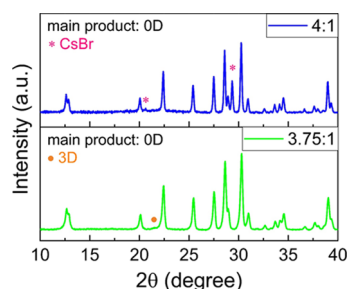


**Figure 3.** XRD patterns of powders precipitated from 3.75:1 (green pattern) and 4:1 (blue pattern) CsBr:PbBr<sub>2</sub> precursor solutions in DMSO.

CsPbBr<sub>3</sub>-free Cs<sub>4</sub>PbBr<sub>6</sub> from DMSO and DMF solutions could be challenging. It is worth mentioning that the dried powders precipitated from all the different ratios were green-emitting under the UV lamp.

**ssNMR on Cs-Pb-Br Powders.** We carried out <sup>207</sup>Pb and <sup>133</sup>Cs solid-state nuclear magnetic resonance (ssNMR) analyses to explore the composition of our precipitates. ssNMR is a powerful characterization tool that can distinguish between different crystal structures of the same material,<sup>37</sup> and it can also identify the formation of amorphous and hydrated hybrid perovskite phases.<sup>38–40</sup> Since it is well known that the main drawback for NMR is the intrinsic poor sensitivity, we first checked the sensitivity of ssNMR in detecting perovskite impurities in the Cs-based perovskites. For this purpose, two samples were used, specifically, 3D CsPbBr<sub>3</sub> with very low OD Cs<sub>4</sub>PbBr<sub>6</sub> impurity (1:1 DMF) and OD Cs<sub>4</sub>PbBr<sub>6</sub> with very low 3D CsPbBr<sub>3</sub> impurity (3.75:1 DMSO) as suggested by their XRD patterns shown in Figure 2a (black pattern) and Figure 3 (green pattern), respectively. All ssNMR data are summarized in Table 1. The detection of the impurity phases was successful

**Table 1.** Summary of Powder XRD and <sup>133</sup>Cs and <sup>207</sup>Pb ssNMR Analysis on Three Different Samples<sup>a</sup>

sample CsBr:PbBr <sub>2</sub> solvent	powder XRD	<sup>133</sup> Cs ssNMR	<sup>207</sup> Pb ssNMR
1:1 DMF	3D + OD impurity	3D (120 ppm) + OD impurity	3D only (246 ppm, <sup>1</sup> J <sub>Pb-Br</sub> = 2425 Hz)
3.75:1 DMSO	OD + 3D impurity	OD (354 and 233.6 ppm) + 3D impurity	OD only (−373 ppm, <sup>1</sup> J <sub>Pb-Br</sub> = 2050 Hz)
4:1 DMSO	OD + CsBr	OD + CsBr (268 ppm)	OD only

<sup>a</sup>In brackets, the  $\delta_{\text{iso}}$  (ppm) of the different phases is reported. For the <sup>207</sup>Pb signal, the scalar coupling constant <sup>1</sup>J<sub>Pb-Br</sub> typical for these systems is also included.<sup>41</sup>

by <sup>133</sup>Cs ssNMR (Figure 4a) but not by <sup>207</sup>Pb ssNMR (Figure 4b) despite the first nuclide being quadrupolar ( $I = 7/2$ , natural abundance = 100%) while <sup>207</sup>Pb is not ( $I = 1/2$ , natural abundance = 22.6%), suggesting higher sensitivity of <sup>133</sup>Cs ssNMR compared to its <sup>207</sup>Pb counterpart in these highly crystalline materials. It is worth noticing that the Pb signals show a fine structure with well-defined components of the multiplet originating from coupling between <sup>207</sup>Pb and the six <sup>79/81</sup>Br atoms ( $I = 3/2$ , natural abundances of <sup>79</sup>Br = 50.54% and <sup>81</sup>Br = 49.46%), surrounding the metal ions in an octahedral geometry, as already reported for similar Cl complexes.<sup>41</sup> We found that <sup>133</sup>Cs ssNMR was also able to distinguish between two kinds of Cs atoms, lying in different environments in the OD crystal structure<sup>42</sup> with a ratio between

2:1 and 3:1, as expected from the OD unit cell. Moving to the “3D-free” OD sample (4:1 DMSO), the XRD pattern of which we report in Figure 3 (blue pattern), <sup>133</sup>Cs ssNMR identified CsBr ( $\delta_{\text{iso}} = 268$  ppm), which was also detected by XRD. Importantly, <sup>133</sup>Cs ssNMR did not detect any 3D impurity in agreement with powder XRD.

**Optical and Compositional Analysis of Green-Emitting Cs<sub>4</sub>PbBr<sub>6</sub> Powder.** We focused on the “3D-free” OD powder (4:1 DMSO). Although XRD (Figure 3, blue pattern) and ssNMR (Figure 4, blue trace) did not detect any 3D impurity in this sample, diffuse reflectance measurements, as plotted in Figure 5a, showed absorption throughout the green region with a matching PLE (Figure S5) and a single PL emission peak at 520 nm (Figure 5a). It is worth mentioning that, in the case of our OD powders with (3.75:1 DMSO) or without (4:1 DMSO) detectable 3D impurity, the as-precipitated wet powders are nonemissive under the UV lamp. However, they turn green-emitting after some time, whether the precipitate is left in solution, dried in a vacuum oven at 40 °C, or under N<sub>2</sub> at room temperature.

An inspection of the 4:1 DMSO sample with an optical microscope under white light (Figure S6a) and UV light (Figure S6b) revealed that the green emission is localized in bright spots scattered across the sample. This observation was further confirmed by a confocal PL microscope using 488 nm excitation (Figure 5b). The PL spectrum collected from a local area containing several emission centers peaked at ~520 nm (Figure S7), in agreement with the PL spectrum in Figure 5a. A spatial distribution of the emitting centers in three dimensions was obtained through the series of *z* slices of the ~40 × 40 × 5 micron volume of the sample (Figure S8). It further confirms that the emission originates from the localized spots in the sample, which are unevenly distributed across the sample. The size of the emissive domains is submicron, and resolving their shape is beyond the spatial resolution of the microscope used.

Elemental analysis of the powder was done using X-ray photoelectron spectroscopy (XPS) and energy-dispersive X-ray spectroscopy (EDS), and the compositional data is listed in Table S1. Both XPS and EDS analyses reveal that the sample is Br-deficient. This Br deficiency contradicts most reports on green-emitting OD materials where samples were reported to be Br-rich with Pb:Br ratios up to 1:7.4.<sup>43</sup> The bromine deficiency in our OD sample could be due to incorporation of other phases with lower bromine content. Next, we measured the separation between the onset of valence band maxima (VBM) and Fermi level shown in Figure 6a. We observed only a small shift when compared to reported VBM onsets of 3D CsPbBr<sub>3</sub>, suggesting a possible 3D or 3D-like impurity in our OD sample.<sup>44</sup> Similarly, high-resolution transmission electron microscopy (HRTEM) analysis on the OD sample detected a domain with lattice spacing of 5.8 Å that is indicative of 3D-like nature (Figure 6b,c). Based on elemental analysis of different particles in the 4:1 DMSO sample, Cs<sub>4</sub>PbBr<sub>6</sub> and the impurity CsBr particles were observed as individual entities and not as a composite (Figure S9).

**Origin of the Green Emission.** While bromine vacancy ( $V_{\text{Br}}$ ) transition level energy in the Cs<sub>4</sub>PbBr<sub>6</sub> was calculated by Yin et al.<sup>13</sup> to be 2.3 eV above the VBM, matching the green emission and, recently,  $V_{\text{Br}}$  was instead suggested to form a shallow defect level.<sup>45</sup> In addition, as we have previously reported,<sup>12</sup> the intense and sharp emission and the absence of a Stokes shift does not match with deep-trap emission.

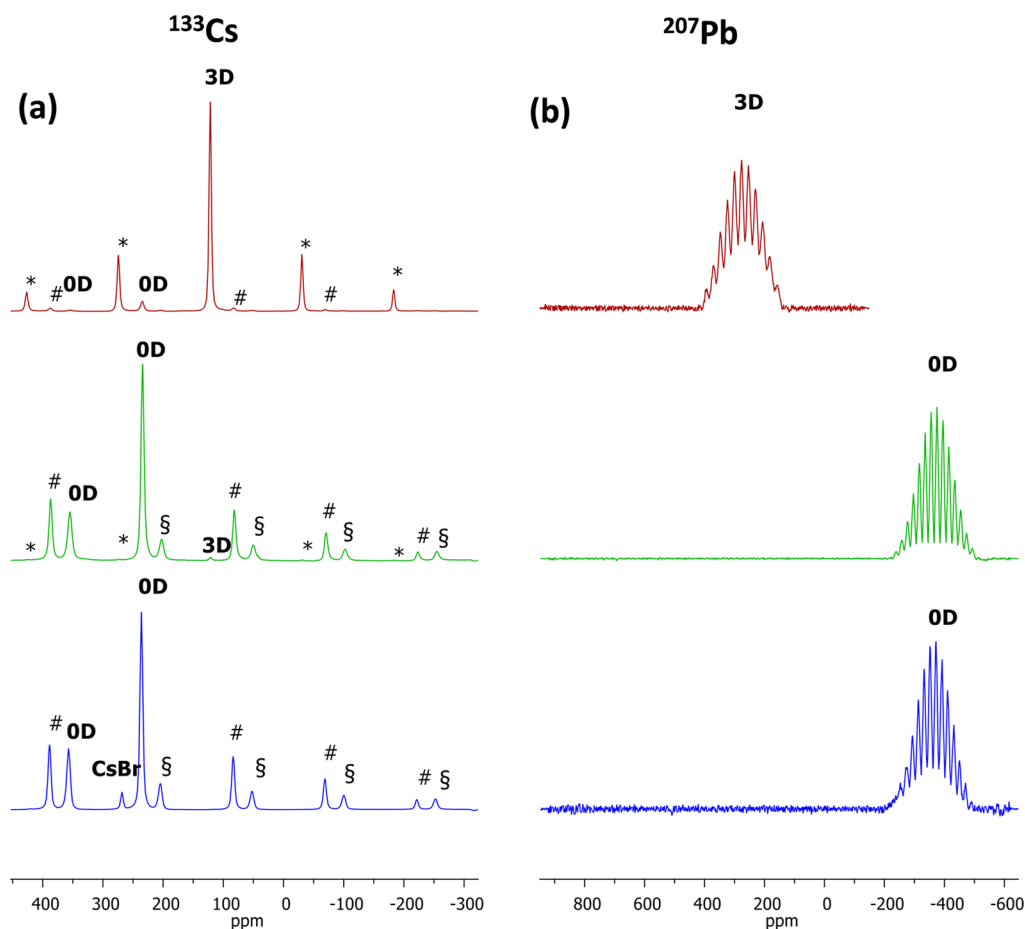


**Figure 4.** (a)  $^{133}\text{Cs}$  and (b)  $^{207}\text{Pb}$  ssNMR spectra (10 kHz MAS, 11.75 T, 312 K) of the samples 1:1 DMF (red trace), 3.75:1 DMSO (green trace), and 4:1 DMSO (blue trace). The asterisks (\*) mark the spinning sidebands (SSBs) of the 3D phase signal, the section signs (§) mark the SSB of the less intense 0D peak, and the pound signs (#) mark the SSB of the more intense 0D peak.

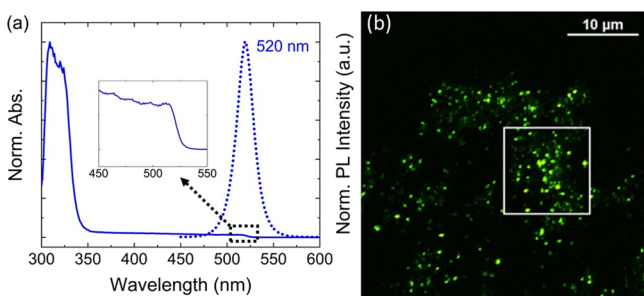


**Figure 5.** (a) Optical absorption (solid line) of the 4:1 DMSO powder sample obtained by converting reflectance ( $R$ ) to absorption using the Kubelka–Munk equation,<sup>6</sup>  $F(R) = (1 - R)^2/2R$ , and PL emission (dotted line) at the excitation wavelength of 405 nm. (b) Confocal PL microscopy image recorded with 488 nm excitation; the PL spectrum from an area highlighted by the white square is shown in Figure S7.

Therefore, impurity emission would be more reasonable as the origin of the green emission. Impurity emission is in line with our confocal PL microscopy, VBM analysis, and HRTEM findings. 3D  $\text{CsPbBr}_3$  could be the impurity source of the green PL emission as nonquantum-confined nanocrystals (> 8 nm) do indeed emit at around 2.39–2.41 eV.<sup>46</sup> However, in agreement with Wang et al.,<sup>47</sup> it is expected that the 3D  $\text{CsPbBr}_3$  impurity might not be the only origin of the green emission. For instance, a previous report detected quantum-

confined  $\sim 3$  nm  $\text{CsPbBr}_3$  nanocrystals embedded within larger-sized  $\text{Cs}_4\text{PbBr}_6$  using HRTEM; however, the sample was green-emitting at 520 nm,<sup>22</sup> defying reported PL values for such small  $\text{CsPbBr}_3$  nanocrystals.<sup>46</sup> In fact, PLQYs of our 0D samples with detectable 3D impurity (3.75:1 DMSO) and 3D-free (4:1 DMSO) were 25 and 50%, respectively.

Other than the known perovskite or perovskite-related phases of 3D ( $\text{CsPbBr}_3$ ), 2D ( $\text{CsPb}_2\text{Br}_5$ ), and 0D ( $\text{Cs}_4\text{PbBr}_6$ ), Song et al.<sup>48</sup> reported the synthesis of a  $\text{Cs}_2\text{PbBr}_4$  material, which they described as a 2D sheet of corner-sharing  $[\text{PbBr}_6]^{4-}$  octahedra passivated by  $\text{Cs}^+$  ions, exhibiting an absorbance and emission in the green region of the visible spectrum. This phase has not been previously reported in the phase diagram of this ternary Cs–Pb–Br system, and the synthesis of a bulk sample of  $\text{Cs}_2\text{PbBr}_4$  appears to be challenging as the phase was suggested to be thermodynamically unstable.<sup>49</sup> However, this 2D sheet of corner-shared  $[\text{PbBr}_6]^{4-}$  octahedra is in essence a monolayer of 3D  $\text{CsPbBr}_3$ . Furthermore, the 2D Ruddlesden–Popper (RP) phase of  $\text{Cs}_{n+1}\text{Pb}_n\text{Br}_{3n+1}$  with  $n = 1$  or 2 has also been detected as an impurity within 3D  $\text{CsPbBr}_3$  nanosheets.<sup>50</sup> Theoretically, at  $n = 1$ , the  $\text{Cs}_2\text{PbBr}_4$  layer is predicted to be a direct band-gap material, and upon introducing spin–orbit coupling (SOC) combined with a hybrid function (HSE), Yang et al.<sup>51</sup> calculated its band gap to be 2.29 eV.

In pure 2D perovskites such as 2D  $\text{MA}_2\text{PbI}_4$ , the difference between the band gaps of a monolayer and bulk material is

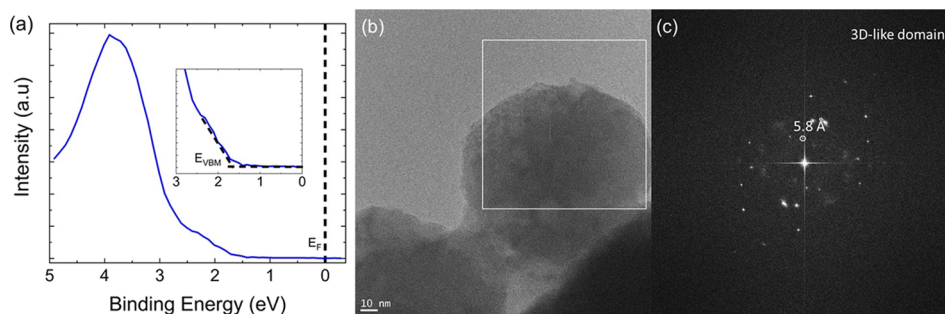


**Figure 6.** (a) XPS results on the 4:1 DMSO sample showing the separation between the onset of valence band maxima (VBM) and Fermi level. (b) HRTEM image and (c) corresponding fast Fourier transform (FFT) of the white square area showing lattice spacing of 5.8 Å.

theoretically calculated to be only 0.01 eV.<sup>52</sup> Experimentally, unlike the quasi-2D, for example,  $(\text{BA})_2(\text{MA})_{n-1}\text{Pb}_n\text{I}_{3n+1}$  (BA = butylammonium) that possesses a considerable blueshift in the PL peak position as the number of layers ( $n$ ) decreases,<sup>53</sup> pure 2D perovskites showed insignificant differences.<sup>54,55</sup> Hence, a 2D perovskite structure with a small Cs cation as an interlayer spacer could explain the narrow range of PL (515 to 524 nm)<sup>12,56</sup> reported for the emissive 0D single crystals, powders, and nanocrystals. The proposed  $\text{Cs}_2\text{PbBr}_4$  is different from 3–5 layered  $\text{CsPbBr}_3$  nanosheets or nanoplatelets that usually emit between 440 and 460 nm.<sup>57,58</sup> This discrepancy in the PL peak position could be attributed to the fact that, in the case of nanosheets and nanoplatelets, their top and bottom surfaces are covered with large organic cations such as oleylammonium or octylammonium, and hence, they could be considered as quasi-2D perovskites, leading to the pronounced blueshift in their emissions.

This hypothesis of 2D  $\text{Cs}_2\text{PbBr}_4$  inclusions being responsible for the absorbance and emission in the green region of the visible spectrum is in agreement with work by Liu et al.<sup>59</sup> where they suggested the formation of  $[\text{PbBr}_4]^{2-}$  intermediates (in the form of sheet structures observed in TEM) during the transformation of  $\text{CsPbBr}_3$  nanocrystals to  $\text{Cs}_4\text{PbBr}_6$  nanocrystals. It is possible that the 0D matrix stabilizes this 2D  $\text{Cs}_{n+1}\text{Pb}_n\text{Br}_{3n+1}$  with the  $n = 1$  ( $\text{Cs}_2\text{PbBr}_4$ ) phase similar to what was detected in 3D nanosheets.<sup>50</sup>

## CONCLUSIONS

To summarize, a mixture of  $\text{CsBr-PbBr}_2$  salts dissolved in DMSO and DMF results in the formation of different lead bromide species with a solvent-dependent solvodynamic radius of the species. Solutions in DMSO feature smaller species ( $\sim 1$  nm of solvodynamic size) compared to the solutions in DMF, which is likely due to the stronger coordination of DMSO to  $\text{Pb}^{2+}$  compared to DMF. The size of lead bromide species influences the composition of the Cs-Pb-Br precipitates upon addition of the antisolvent: smaller species favor the formation of the  $\text{Cs}_4\text{PbBr}_6$  phase, while larger species template the precipitation of  $\text{CsPbBr}_3$ . Overall, 0D  $\text{Cs}_4\text{PbBr}_6$  has a higher tendency to be precipitated out from solutions with stronger coordinating solvents to  $\text{Pb}^{2+}$ , lower absolute concentration of the precursors, and higher CsBr: $\text{PbBr}_2$  ratios, compared to its 3D  $\text{CsPbBr}_3$  counterpart. We have discussed a possible origin of the green emission in the wide-band-gap  $\text{Cs}_4\text{PbBr}_6$  and concluded that 3D impurities might not be the only source of the emission and high PLQY. Alternatively, an impurity of 2D  $\text{Cs}_2\text{PbBr}_4$  has been proposed, but no conclusive experimental evidence of its existence was obtained. Our work highlights the

importance of the less-investigated small cation spacers (e.g., Cs or MA) in 2D perovskites. Future work would target understanding the formation mechanism of  $\text{Cs}_2\text{PbBr}_4$  as an impurity within  $\text{Cs}_4\text{PbBr}_6$ .

## ASSOCIATED CONTENT

### Supporting Information

The Supporting Information is available free of charge on the ACS Publications website at DOI: [10.1021/acs.chemmater.9b02944](https://doi.org/10.1021/acs.chemmater.9b02944).

PLE, PL, and DLS of  $\text{PbBr}_2$ -only solutions, optical images, confocal PL microscopy volume view, and high-angle annular dark-field (HAADF), and elemental analysis of the 4:1 DMSO sample (PDF)

## AUTHOR INFORMATION

### Corresponding Authors

\*E-mail: [liberato.manna@iit.it](mailto:liberato.manna@iit.it) (L.M.).

\*E-mail: [ahmed.abdelhady@iit.it](mailto:ahmed.abdelhady@iit.it) (A.L.A.).

### ORCID

Daniela Maggioni: 0000-0001-5201-4824

Dmitry Baranov: 0000-0001-6439-8132

Zhiya Dang: 0000-0003-2238-540X

Mirko Prato: 0000-0002-2188-8059

Liberato Manna: 0000-0003-4386-7985

Ahmed L. Abdelhady: 0000-0002-6637-8853

### Author Contributions

The manuscript was written through contributions of all authors. All authors have given approval to the final version of the manuscript.

### Notes

The authors declare no competing financial interest.

## ACKNOWLEDGMENTS

The research leading to these results has received funding from the European Union 7th Framework Program under grant agreement no. 614897 (ERC Consolidator Grant “TRANS-NANO”). The work of D.B. was supported by the European Union’s Horizon 2020 research and innovation program under the Marie Skłodowska-Curie grant agreement no. 794560 (RETAIN). We thank Dr. Federico Locardi and Dr. Guilherme Almeida for helpful discussions and suggestions and Dr. Francesca Benevelli (BrukerBiospin) and Pasquale Illiano (University of Milan) for NMR technical assistance.

## REFERENCES

- (1) Saidaminov, M. I.; Mohammed, O. F.; Bakr, O. M. Low-Dimensional-Networked Metal Halide Perovskites: The Next Big Thing. *ACS Energy Lett.* **2017**, *2*, 889–896.
- (2) Lin, H.; Zhou, C.; Tian, Y.; Siegrist, T.; Ma, B. Low-Dimensional Organometal Halide Perovskites. *ACS Energy Lett.* **2017**, 54–62.
- (3) Shi, E.; Gao, Y.; Finkenauer, B. P.; Akriti; Coffey, A. H.; Dou, L. Two-Dimensional Halide Perovskite Nanomaterials and Heterostructures. *Chem. Soc. Rev.* **2018**, *47*, 6046–6072.
- (4) Gao, P.; Bin Mohd Yusoff, A. R.; Nazeeruddin, M. K. Dimensionality Engineering of Hybrid Halide Perovskite Light Absorbers. *Nat. Commun.* **2018**, *9*, 5028.
- (5) Yuan, Z.; Zhou, C.; Tian, Y.; Shu, Y.; Messier, J.; Wang, J. C.; van de Burgt, L. J.; Kountouriotis, K.; Xin, Y.; Holt, E.; Schanze, K.; Clark, R.; Siegrist, T.; Ma, B. One-Dimensional Organic Lead Halide Perovskites with Efficient Bluish White-Light Emission. *Nat. Commun.* **2017**, *8*, 14051.
- (6) Liu, M.; Zhao, J.; Luo, Z.; Sun, Z.; Pan, N.; Ding, H.; Wang, X. Unveiling Solvent-Related Effect on Phase Transformations in CsBr-PbBr<sub>2</sub> System: Coordination and Ratio of Precursors. *Chem. Mater.* **2018**, *30*, 5846–5852.
- (7) Zhao, Y.; Zhu, K. Organic-Inorganic Hybrid Lead Halide Perovskites for Optoelectronic and Electronic Applications. *Chem. Soc. Rev.* **2016**, *45*, 655–689.
- (8) Adinolfi, V.; Yuan, M.; Comin, R.; Thibau, E. S.; Shi, D.; Saidaminov, M. I.; Kanjanaboos, P.; Kopilovic, D.; Hoogland, S.; Lu, Z.-H.; Bakr, O. M.; Sargent, E. H. The in-Gap Electronic State Spectrum of Methylammonium Lead Iodide Single-Crystal Perovskites. *Adv. Mater.* **2016**, *28*, 3406–3410.
- (9) Cha, J.-H.; Han, J. H.; Yin, W.; Park, C.; Park, Y.; Ahn, T. K.; Cho, J. H.; Jung, D.-Y. Photoresponse of CsPbBr<sub>3</sub> and Cs<sub>4</sub>PbBr<sub>6</sub> Perovskite Single Crystals. *J. Phys. Chem. Lett.* **2017**, *8*, 565–570.
- (10) Yin, J.; Zhang, Y.; Bruno, A.; Soci, C.; Bakr, O. M.; Brédas, J.-L.; Mohammed, O. F. Intrinsic Lead Ion Emissions in Zero-Dimensional Cs<sub>4</sub>PbBr<sub>6</sub> Nanocrystals. *ACS Energy Lett.* **2017**, *2*, 2805–2811.
- (11) Zhang, Y.; Saidaminov, M. I.; Dursun, I.; Yang, H.; Murali, B.; Alarousu, E.; Yengel, E.; Alshankiti, B. A.; Bakr, O. M.; Mohammed, O. F. Zero-Dimensional Cs<sub>4</sub>PbBr<sub>6</sub> Perovskite Nanocrystals. *J. Phys. Chem. Lett.* **2017**, *8*, 961–965.
- (12) Akkerman, Q. A.; Abdelhady, A. L.; Manna, L. Zero-Dimensional Cesium Lead Halides: History, Properties, and Challenges. *J. Phys. Chem. Lett.* **2018**, *9*, 2326–2337.
- (13) Yin, J.; Yang, H.; Song, K.; El-Zohry, A. M.; Han, Y.; Bakr, O. M.; Brédas, J.-L.; Mohammed, O. F. Point Defects and Green Emission in Zero-Dimensional Perovskites. *J. Phys. Chem. Lett.* **2018**, *9*, 5490–5495.
- (14) Seth, S.; Samanta, A. Fluorescent Phase-Pure Zero-Dimensional Perovskite-Related Cs<sub>4</sub>PbBr<sub>6</sub> Microdisks: Synthesis and Single-Particle Imaging Study. *J. Phys. Chem. Lett.* **2017**, *8*, 4461–4467.
- (15) De Bastiani, M.; Dursun, I.; Zhang, Y.; Alshankiti, B. A.; Miao, X.-H.; Yin, J.; Yengel, E.; Alarousu, E.; Turedi, B.; Almutlaq, J. M.; Saidaminov, M. I.; Mitra, S.; Gereige, I.; AlSaggaf, A.; Zhu, Y.; Han, Y.; Roqan, I. S.; Brédas, J.-L.; Mohammed, O. F.; Bakr, O. M. Inside Perovskites: Quantum Luminescence from Bulk Cs<sub>4</sub>PbBr<sub>6</sub> Single Crystals. *Chem. Mater.* **2017**, *29*, 7108–7113.
- (16) Wells, H. L. Über Die Cäsium- Und Kalium-Bleihalogenide. *Z. Anorg. Chem.* **1893**, *3*, 195–210.
- (17) Nikl, M.; Mihokova, E.; Nitsch, K.; Somma, F.; Giampaolo, C.; Pazzi, G. P.; Fabeni, P.; Zazubovich, S. Photoluminescence of Cs<sub>4</sub>PbBr<sub>6</sub> Crystals and Thin Films. *Chem. Phys. Lett.* **1999**, *306*, 280–284.
- (18) Kondo, S.; Amaya, K.; Saito, T. Localized Optical Absorption in Cs<sub>4</sub>PbBr<sub>6</sub>. *J. Phys.: Condens. Matter* **2002**, *14*, 2093–2099.
- (19) Akkerman, Q. A.; Park, S.; Radicchi, E.; Nunzi, F.; Mosconi, E.; De Angelis, F.; Brescia, R.; Rastogi, P.; Prato, M.; Manna, L. Nearly Monodisperse Insulator Cs<sub>4</sub>PbX<sub>6</sub> (X = Cl, Br, I) Nanocrystals, Their Mixed Halide Compositions, and Their Transformation into CsPbX<sub>3</sub> Nanocrystals. *Nano Lett.* **2017**, *17*, 1924–1930.
- (20) Quan, L. N.; Quintero-Bermudez, R.; Voznyy, O.; Walters, G.; Jain, A.; Fan, J. Z.; Zheng, X.; Yang, Z.; Sargent, E. H. Highly Emissive Green Perovskite Nanocrystals in a Solid State Crystalline Matrix. *Adv. Mater.* **2017**, *29*, 1605945.
- (21) Xu, J.; Huang, W.; Li, P.; Onken, D. R.; Dun, C.; Guo, Y.; Ucer, K. B.; Lu, C.; Wang, H.; Geyer, S. M.; Williams, R. T.; Carroll, D. L. Imbedded Nanocrystals of CsPbBr<sub>3</sub> in Cs<sub>4</sub>PbBr<sub>6</sub>: Kinetics, Enhanced Oscillator Strength, and Application in Light-Emitting Diodes. *Adv. Mater.* **2017**, *29*, 1703703.
- (22) Chen, X.; Zhang, F.; Ge, Y.; Shi, L.; Huang, S.; Tang, J.; Lv, Z.; Zhang, L.; Zou, B.; Zhong, H. Centimeter-Sized Cs<sub>4</sub>PbBr<sub>6</sub> Crystals with Embedded CsPbBr<sub>3</sub> Nanocrystals Showing Superior Photoluminescence: Nonstoichiometry Induced Transformation and Light-Emitting Applications. *Adv. Funct. Mater.* **2018**, 1706567.
- (23) Xuan, T.; Lou, S.; Huang, J.; Cao, L.; Yang, X.; Li, H.; Wang, J. Monodisperse and Brightly Luminescent CsPbBr<sub>3</sub>/Cs<sub>4</sub>PbBr<sub>6</sub> Perovskite Composite Nanocrystals. *Nanoscale* **2018**, *10*, 9840–9844.
- (24) Riesen, N.; Lockrey, M.; Badek, K.; Riesen, H. On the Origins of the Green Luminescence in the “Zero-Dimensional Perovskite” Cs<sub>4</sub>PbBr<sub>6</sub>: Conclusive Results from Cathodoluminescence Imaging. *Nanoscale* **2019**, *11*, 3925–3932.
- (25) Ling, Y.; Tan, L.; Wang, X.; Zhou, Y.; Xin, Y.; Ma, B.; Hanson, K.; Gao, H. Composite Perovskites of Cesium Lead Bromide for Optimized Photoluminescence. *J. Phys. Chem. Lett.* **2017**, *8*, 3266–3271.
- (26) Baranov, D.; Toso, S.; Imran, M.; Manna, L. Investigation into the Photoluminescence Red Shift in Cesium Lead Bromide Nanocrystal Superlattices. *J. Phys. Chem. Lett.* **2019**, *10*, 655–660.
- (27) Yoon, S. J.; Stamplecoskie, K. G.; Kamat, P. V. How Lead Halide Complex Chemistry Dictates the Composition of Mixed Halide Perovskites. *J. Phys. Chem. Lett.* **2016**, *7*, 1368–1373.
- (28) Oldenburg, K.; Vogler, A. Electronic Spectra and Photochemistry of Tin(II), Lead(II), Antimony(III), and Bismuth(III) Bromide Complexes in Solution. *Z. Naturforsch., B* **1993**, *48*, 1519–1523.
- (29) Rahimnejad, S.; Kovalenko, A.; Forés, S. M.; Aranda, C.; Guerrero, A. Coordination Chemistry Dictates the Structural Defects in Lead Halide Perovskites. *ChemPhysChem* **2016**, *17*, 2795–2798.
- (30) Hamill, J. C., Jr.; Schwartz, J.; Loo, Y.-L. Influence of Solvent Coordination on Hybrid Organic–Inorganic Perovskite Formation. *ACS Energy Lett.* **2018**, *3*, 92–97.
- (31) Wu, Y.; Islam, A.; Yang, X.; Qin, C.; Liu, J.; Zhang, K.; Peng, W.; Han, L. Retarding the Crystallization of PbI<sub>2</sub> for Highly Reproducible Planar-Structured Perovskite Solar Cells Via Sequential Deposition. *Energy Environ. Sci.* **2014**, *7*, 2934–2938.
- (32) Yan, K.; Long, M.; Zhang, T.; Wei, Z.; Chen, H.; Yang, S.; Xu, J. Hybrid Halide Perovskite Solar Cell Precursors: Colloidal Chemistry and Coordination Engineering Behind Device Processing for High Efficiency. *J. Am. Chem. Soc.* **2015**, *137*, 4460–4468.
- (33) McMeekin, D. P.; Wang, Z.; Rehman, W.; Pulvirenti, F.; Patel, J. B.; Noel, N. K.; Johnston, M. B.; Marder, S. R.; Herz, L. M.; Snaith, H. J. Crystallization Kinetics and Morphology Control of Formamidinium-Cesium Mixed-Cation Lead Mixed-Halide Perovskite Via Tunability of the Colloidal Precursor Solution. *Adv. Mater.* **2017**, *29*, 1607039.
- (34) Wei, Z.; Perumal, A.; Su, R.; Sushant, S.; Xing, J.; Zhang, Q.; Tan, S. T.; Demir, H. V.; Xiong, Q. Solution-Processed Highly Bright and Durable Cesium Lead Halide Perovskite Light-Emitting Diodes. *Nanoscale* **2016**, *8*, 18021–18026.
- (35) Stevenson, J.; Sorenson, B.; Subramaniam, V. H.; Raiford, J.; Khlyabich, P. P.; Loo, Y.-L.; Clancy, P. Mayer Bond Order as a Metric of Complexation Effectiveness in Lead Halide Perovskite Solutions. *Chem. Mater.* **2016**, *29*, 2435–2444.
- (36) Xu, Y.; Zhang, Q.; Lv, L.; Han, W.; Wu, G.; Yang, D.; Dong, A. Synthesis of Ultrasmall CsPbBr<sub>3</sub> Nanoclusters and Their Transformation to Highly Deep-Blue-Emitting Nanoribbons at Room Temperature. *Nanoscale* **2017**, 17248.

- (37) Bureau, B.; Silly, G.; Buzaré, J. Y. CP-MAS  $^{207}\text{Pb}$  with  $^{19}\text{F}$  Decoupling NMR Spectroscopy: Medium Range Investigation in Fluoride Materials. *Solid State Nucl. Magn. Reson.* **1999**, *15*, 79–89.
- (38) Rosales, B. A.; Men, L.; Cady, S. D.; Hanrahan, M. P.; Rossini, A. J.; Vela, J. Persistent Dopants and Phase Segregation in Organolead Mixed-Halide Perovskites. *Chem. Mater.* **2016**, *28*, 6848–6859.
- (39) Askar, A. M.; Bernard, G. M.; Wiltshire, B.; Shankar, K.; Michaelis, V. K. Multinuclear Magnetic Resonance Tracking of Hydro, Thermal and Hydrothermal Decomposition of  $\text{CH}_3\text{NH}_3\text{PbI}_3$ . *J. Phys. Chem. C* **2017**, *121*, 1013–1024.
- (40) Rosales, B. A.; Hanrahan, M. P.; Boote, B. W.; Rossini, A. J.; Smith, E. A.; Vela, J. Lead Halide Perovskites: Challenges and Opportunities in Advanced Synthesis and Spectroscopy. *ACS Energy Lett.* **2017**, *2*, 906–914.
- (41) Wrackmeyer, B.; Horchler, K.  $^{207}\text{Pb}$ -NMR Parameters. In *Annual Reports on NMR Spectroscopy*; Webb, G. A., Ed.; Academic Press: 1990; Vol. 22, pp 249–306.
- (42) Hu, M.; Ge, C.; Yu, J.; Feng, J. Mechanical and Optical Properties of  $\text{Cs}_x\text{BX}_6$  (B = Pb, Sn; X = Cl, Br, I) Zero-Dimension Perovskites. *J. Phys. Chem. C* **2017**, *121*, 27053–27058.
- (43) Yang, H.; Zhang, Y.; Pan, J.; Yin, J.; Bakr, O. M.; Mohammed, O. F. Room-Temperature Engineering of All-Inorganic Perovskite Nanocrystals with Different Dimensionalities. *Chem. Mater.* **2017**, *29*, 8978–8982.
- (44) Endres, J.; Egger, D. A.; Kulbak, M.; Kerner, R. A.; Zhao, L.; Silver, S. H.; Hodes, G.; Rand, B. P.; Cahen, D.; Kronik, L.; Kahn, A. Valence and Conduction Band Densities of States of Metal Halide Perovskites: A Combined Experimental–Theoretical Study. *J. Phys. Chem. Lett.* **2016**, *7*, 2722–2729.
- (45) Jung, Y.-K.; Calbo, J.; Park, J.-S.; Wahlley, L. D.; Kim, S.; Walsh, A. Luminescence of Polybromide Defects in  $\text{Cs}_4\text{PbBr}_6$ . *ChemRxiv* **2019**, DOI: [10.26434/chemrxiv.7629467](https://doi.org/10.26434/chemrxiv.7629467).
- (46) Almeida, G.; Goldoni, L.; Akkerman, Q.; Dang, Z.; Khan, A. H.; Marras, S.; Moreels, I.; Manna, L. Role of Acid-Base Equilibria in the Size, Shape, and Phase Control of Cesium Lead Bromide Nanocrystals. *ACS Nano* **2018**, *12*, 1704–1711.
- (47) Wang, K.-H.; Yang, J.-N.; Ni, Q.-K.; Yao, H.-B.; Yu, S.-H. Metal Halide Perovskite Supercrystals: Gold–Bromide Complex Triggered Assembly of  $\text{CsPbBr}_3$  Nanocubes. *Langmuir* **2018**, *34*, 595–602.
- (48) Song, J.; Xu, L.; Li, J.; Xue, J.; Dong, Y.; Li, X.; Zeng, H. Monolayer and Few-Layer All-Inorganic Perovskites as a New Family of Two-Dimensional Semiconductors for Printable Optoelectronic Devices. *Adv. Mater.* **2016**, *28*, 4861–4869.
- (49) Li, J.; Yu, Q.; He, Y.; Stoumpos, C. C.; Niu, G.; Trimarchi, G. G.; Guo, H.; Dong, G.; Wang, D.; Wang, L.; Kanatzidis, M. G.  $\text{Cs}_2\text{PbI}_2\text{Cl}_2$ , All-Inorganic Two-Dimensional Ruddlesden–Popper Mixed Halide Perovskite with Optoelectronic Response. *J. Am. Chem. Soc.* **2018**, *140*, 11085–11090.
- (50) Yu, Y.; Zhang, D.; Yang, P. Ruddlesden–Popper Phase in Two-Dimensional Inorganic Halide Perovskites: A Plausible Model and the Supporting Observations. *Nano Lett.* **2017**, *17*, 5489–5494.
- (51) Yang, J.-H.; Yuan, Q.; Jakobson, B. I. Chemical Trends of Electronic Properties of Two-Dimensional Halide Perovskites and Their Potential Applications for Electronics and Optoelectronics. *J. Phys. Chem. C* **2016**, *120*, 24682–24687.
- (52) Zhu, X.; Xu, Z.; Zuo, S.; Feng, J.; Wang, Z.; Zhang, X.; Zhao, K.; Zhang, J.; Liu, H.; Priya, S.; Liu, S. F.; Yang, D. Vapor-Fumigation for Record Efficiency Two-Dimensional Perovskite Solar Cells with Superior Stability. *Energy Environ. Sci.* **2018**, *11*, 3349–3357.
- (53) Stoumpos, C. C.; Cao, D. H.; Clark, D. J.; Young, J.; Rondinelli, J. M.; Jang, J. I.; Hupp, J. T.; Kanatzidis, M. G. Ruddlesden–Popper Hybrid Lead Iodide Perovskite 2D Homologous Semiconductors. *Chem. Mater.* **2016**, *28*, 2852–2867.
- (54) Dou, L.; Wong, A. B.; Yu, Y.; Lai, M.; Kornienko, N.; Eaton, S. W.; Fu, A.; Bischak, C. G.; Ma, J.; Ding, T.; Ginsberg, N. S.; Wang, L.-W.; Alivisatos, A. P.; Yang, P. Atomically Thin Two-Dimensional Organic-Inorganic Hybrid Perovskites. *Science* **2015**, *349*, 1518–1521.
- (55) Yin, H.; Jin, L.; Qian, Y.; Li, X.; Wu, Y.; Bowen, M. S.; Kaan, D.; He, C.; Wozniak, D. I.; Xu, B.; Lewis, A. J.; Shen, W.; Chen, K.; Dobreiner, G. E.; Zhao, Y.; Wayland, B. B.; Rao, Y. Excitonic and Confinement Effects of 2D Layered  $(\text{C}_{10}\text{H}_{21}\text{NH}_3)_2\text{PbBr}_4$  Single Crystals. *ACS Appl. Energy Mater.* **2018**, *1*, 1476–1482.
- (56) Almutlaq, J.; Yin, J.; Mohammed, O. F.; Bakr, O. M. The Benefit and Challenges of Zero-Dimensional Perovskites. *J. Phys. Chem. Lett.* **2018**, *9*, 4131–4138.
- (57) Akkerman, Q. A.; Motti, S. G.; Srimath Kandada, A. R.; Mosconi, E.; D’Innocenzo, V.; Bertoni, G.; Marras, S.; Kamino, B. A.; Miranda, L.; De Angelis, F.; Petrozza, A.; Prato, M.; Manna, L. Solution Synthesis Approach to Colloidal Cesium Lead Halide Perovskite Nanoplatelets with Monolayer-Level Thickness Control. *J. Am. Chem. Soc.* **2016**, *138*, 1010–1016.
- (58) Shamsi, J.; Dang, Z.; Bianchini, P.; Canale, C.; Di Stasio, F.; Brescia, R.; Prato, M.; Manna, L. Colloidal Synthesis of Quantum Confined Single Crystal  $\text{CsPbBr}_3$  Nanosheets with Lateral Size Control up to the Micrometer Range. *J. Am. Chem. Soc.* **2016**, *138*, 7240–7243.
- (59) Liu, Z.; Bekenstein, Y.; Ye, X.; Nguyen, S. C.; Swabeck, J.; Zhang, D.; Lee, S.-T.; Yang, P.; Ma, W.; Alivisatos, A. P. Ligand Mediated Transformation of Cesium Lead Bromide Perovskite Nanocrystals to Lead Depleted  $\text{Cs}_4\text{PbBr}_6$  Nanocrystals. *J. Am. Chem. Soc.* **2017**, *139*, 5309–5312.